Enhancing toughness and microstructural memory by coupling crystallinity, elasticity and plasticity in layered materials comprised of liquid crystalline oligomers

Manish Kumar Das and Fernando A. Escobedo*

R. F. Smith School of Chemical and Biomolecular Engineering, Cornell University, Ithaca, New York 14853, United States

Abstract:

Molecular dynamics simulations are used to show that triblock oligomers which are first preassembled into a lamellar phase and then crosslinked, exhibit high extensibility and toughness in response to uniaxial tensile deformation parallel to the layer stacking. A coarse-grained model is adopted based on a coil-rod-coil oligomer capped with crosslinkable units. Upon uniaxial strain, a buckling instability ensues in the uncrosslinked systems, which eventually leads to defective lamellar 'islands' as the stress drops off. In contrast, a toughening behavior, manifested as a 'saw-tooth' stress-strain profile, is observed in the crosslinked systems, which is associated with 'recrystallization' of the rod domains mediated by the inter-layer bonds formed upon crosslinking. It is also shown that this toughening mechanism can be encoded in longer multilayer-spanning oligomer designs that forsake the crosslinking step. These structures, which integrate rigidity, elasticity, and plasticity, could be leveraged to experimentally realize novel materials with shape-memory and self-healing properties.

1. INTRODUCTION

Liquid crystal elastomers (LCEs) are crosslinked networks which combine the orientational ordering of conventional liquid crystals and the elastic behavior of polymers.[1] The orientational ordering of the mesogen units (e.g., in nematic phases) can be induced by changes in thermodynamic conditions,[2] albeit this generally results in polydomain structures. Experimentally, monodomain LCEs have been typically achieved by applying external stimuli, e.g., mechanical,[3] electromagnetic,[4] electric[5] and magnetic fields.[6,7] Furthermore, by incorporating chemically incompatible blocks in the molecular architectures, microphase segregation and translational ordering can be induced in a resulting self-assembled phase (e.g., in lamellar phases).[8,9] Generally, LCEs have also been designed to have a highly non-linear response to mechanical stress, often exhibiting a phenomena called "soft-elasticity",[10] which makes these materials excellent candidates for shape-memory applications.[11–13] In particular, layered (e.g. smectic) LCEs have found applications in designing actuators[14] and artificial muscles.[6] The translational order in these layered structures also provides higher resistance to deformation perpendicular to the layering (hence, resulting in higher "strength") as compared to isotropic elastomers with comparable degree of crosslinking. This is generally a result of increased energy in the solid-like layers for the layered LCEs due to increased lattice strain, while in isotropic elastomers the deformation is more spread out in all directions, leading to a lower global stress in the system.

Rational design of the LCE building blocks for typical applications, which often involve deformations beyond the elastic regime, requires a molecular level understanding of the deformation mechanism. This usually entails cooperative motion of the chains with respect to the direction of the external stimuli. Given the ordering of LCEs, there is also the added effect of the reorientation of the mesogen segments which is generally coupled with the conformational change of the flexible segments. This coupling makes the tensile response of LCEs highly non-trivial, unlike isotropic non-LCE networks where the loss of conformational entropy due to the stretching of the chains is the primary source of stress generation and the concomitant tensile behavior. Molecular dynamics (MD) simulations can be a valuable tool for probing and understanding the molecular mechanisms involved in high strain deformations of materials. For example, atomistic simulations have been used to study tensile deformation in semi-crystalline polyethylene,[15–17] and

to analyze the effect on the high-strain deformation behavior of strain rates, crystalline stacking morphology, interphase topology, etc.[17–19] Coarse grained MD simulations for networks with an ideal or near-ideal diamond connectivity of semiflexible block copolymers have been shown to exhibit a 'sawtooth' tensile response at high strain values.[20–23] The primary underlying mechanism explaining the 'sawtooth' response in those systems is the formation of new microsegregated domains due to unfolding of unentangled hairpin conformations present in such networks. A similarly shaped sawtooth tensile response has been seen in some naturally occurring materials, like abalone shells[24] and muscle protein titin[25], albeit these embodied a different toughening mechanism (i.e., the sequential unravelling of folded domains). More recently, polymeric "double networks" based on two interpenetrating networks, one with short and stiff polymer strands, and the other with long and stretchable polymeric networks, have been demonstrated to show similar sawtooth force extension curves; however, the underpinning mechanism for such a response is macroscopic in nature and relies on local fracture of the first network type.[26] These observations suggest that networks with sawtooth tensile responses can be the basis for designing novel organic "super-tough" materials.

While most of the prior experimental and simulation studies have focused on polymeric networks, we utilize an oligomeric building block for our study, taking advantage of their fast kinetics for self-assembly and defect annealing.[27] And rather than carrying out the crosslinking process in solution prior to self-assembly, our main goal is to demonstrate that the preassembly of these small molecules into a lamellar morphology and subsequent crosslinking can be used as an alternative strategy for designing "super-tough" materials. Specifically, we study the effect of uniaxial tensile deformations in the high strain regime for a coil-rod-coil triblock oligomer self-assembled into a lamellar phase. This model, while intended to be largely generic, is based on a chemistry-explicit system where the "rod" segments are made up of quarterthiophene (4T) units, while each of the "coil" segments consist of four ethylene oxide (EO) units, functionalized with acrylate groups at both ends of the oligomer, which enables generation of crosslinked structures post-assembly. Henceforth, we will be referring to this chemistry as 4T/dEO4. We choose this oligomer architecture as it (and related variants) without the acrylate functionalization have already been synthesized and studied for applications such as mixed-conduction materials,[28–30] including a study

focused on tuning the chain lengths for optimal conduction properties and thermal stability of the lamella phase.[31]

The rest of the paper is organized as follows. In section 2.1, we detail the coarse-grained model used, with the parameters provided in supporting information. In section 2.2, we outline the protocols for preparing the lamellar phase with the coarse-grained oligomers. In section 2.3 and 2.4, we explain the protocols used for preparing the crosslinked configurations and performing tensile deformation, respectively. In section 3, we describe the results for tensile deformation for the uncrosslinked and crosslinked systems for different degrees of crosslinking and strain rates, discussing the mechanism underpinning the behaviors observed. We also include the results of a different, non-crosslinked oligomer system designed to exhibit a tensile response similar to that of the crosslinked lamellar system. In section 4, we provide some concluding remarks on the toughening behavior observed in our system and outline some future directions.

2. MODEL AND METHODS

2.1. Coarse grained model

Due to the relatively large time and length scales required for this study, we used a coarse-grained (CG) model already developed for the 4T/dEO4 oligomer.[32] A schematic depicting the CG mapping for the molecule and the different bead types involved is provided in Figure 1. Each 'T' bead represents a thiophene monomer units and the 'EO1' and 'EO2' types refer to the different types of ethylene oxide units based on their connectivity to the thiophene core, with 'EO2' bead types directly bonded to it. The 'F' bead types represent the acrylate functionalization unit which can undergo crosslinking reactions. The different crosslinking reactions and the corresponding changes to the 'F' bead type are detailed in section 2.3. The non-bonded pairwise interactions between the different types of CG beads are modeled by a cut and shifted LJ potential of the form

$$U_{LJ} = 4\varepsilon\left\{\left(\frac{\sigma}{r}\right)^{12} - \left(\frac{\sigma}{r}\right)^{6} - \left(\frac{\sigma}{r_c}\right)^{12} + \left(\frac{\sigma}{r_c}\right)^{6}\right\} \quad (1)$$

for $r \leq r_c$, and $U_{LJ} = 0$ otherwise with a global LJ cutoff of $r_c = 12$Å. The LJ parameters for each bead type are provided in Table S1. The bonding and angular interactions in the system are modeled with a harmonic potential of the form

$$U_{bond} = k_b(r - r_0)^2 \quad (2)$$

$$U_{angle} = k_\theta(\theta - \theta_0)^2 \quad (3)$$

where k_b, k_θ are the spring force constants (in Kcal/mol) for each bond and angle type respectively, and r_0, θ_0 are the corresponding equilibrium bond lengths and angles. These bonded parameters are provided in Table S2 (for bonds) and S3 (for angles). The high spring constants for bonds and angles between the thiophene (T) beads reflect the 'rigid' nature of this block.

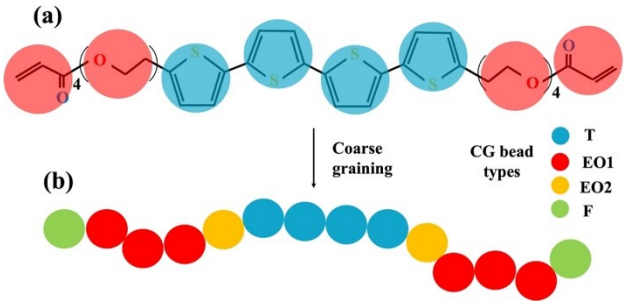

Figure 1. Schematic showing: **(a)** The coarse-grained mapping of 4T/dEO4 with the cyan and red colored CG beads representing the 'rigid' thiophene block and 'flexible' blocks respectively, and **(b)** Different CG bead types that constitute the oligomer molecule, as explained in section 2.1

2.2. Assembly protocol

We prepared a four-layer configuration in a nearly isotropic box ($l_x \sim l_y \sim l_z$) to collect sufficient crosslinking statistics and minimize finite-size effects for high strain deformations. Selected results for a larger six-layer initial configurations are presented in Sec. S7 of the SI which are consistent with those presented for the four-layer case. For preparing the lamellar morphology, we initialize a random configuration of $N_{olig} = 4000$ oligomers in a cubic box at a low density, and perform NPT simulation with LAMMPS[33,34] to allow the system to equilibrate at T = 500K, P = 1atm. The further steps involved in the assembly protocol are:

1) A temperature ramp is applied to cool the system in steps of 10K until it reaches 450K. At each ramp step, 4×10^6 time steps are performed in an NPT ensemble to promote equilibration.

2) When the system reaches 450K, a weak "guiding field" is turned on to align the layers in the z direction for easier mechanical characterization. Details of the implementation of the field is provided in section S3. The system is then cooled again from 450K in steps of 10K, but the simulation time for each ramp step is now increased to 10^7 time steps to allow for proper equilibration near the isotropic-lamella transition. As the objective is to cause the rigid thiophene cores of the oligomer to stack along the z axis, we also henceforth use an anisotropic NPT ensemble to allow the box dimension along the layer stacking direction (z) to vary independently from the lateral dimensions (x and y) and help relax any internal stresses that might be created during the protocol.
3) The transition from isotropic to lamellar phase occurs roughly at 400K, close to experimental observations.[28,31] After the transition, the system is equilibrated with the field turned off for 5×10^6 time steps.
4) The system is then cooled to 300K using an NPT ensemble through a temperature ramp for the subsequent crosslinking and mechanical studies.

2.3. Crosslinking protocol

For preparing the crosslinked configurations, we use a distance-based reaction switching protocol, commonly used in molecular dynamics simulations,[35] modified for reactions involved in UV initiated crosslinking for acrylates.[36–39] In UV based crosslinking, three types of reactions are commonly involved: initiation, propagation and termination, as depicted in figure 2(a). For the termination step, we only use the 'combination' reaction, as shown in figure 2(a), as it has been shown to be the primary mode of termination reaction for acrylates.[40,41] Following earlier works,[36] we first randomly initialize a fraction of the acrylate bead types from type 'F' (unreacted) to type 'R' (reactive), to mimic the initiation reaction. Final crosslinking statistics for different initiation fractions are provided in section 3.1. The different initiation fractions are meant to qualitatively represent the effect of different photoinitiator concentrations, varying intensity and exposure time of UV light, etc., which are known to regulate the initiation process experimentally. The propagation and termination reactions are modeled using the 'fix bond/create/angle' module in LAMMPS, which allows for the formation of bonds and corresponding angular potentials when two coarse grained beads of the prescribed types involved in the reaction are within a certain distance cutoff. The bead types involved in the propagation and termination reactions are depicted

in figure 2(a). The probability of bond formation (in both propagation and termination) when reactive beads are within the distance cutoff is chosen to be 0.5. In our simulations, we also vary the distance cutoff from 3.5Å to 5Å with steps of 0.2 Å and allow for NPT equilibration at each cutoff step to ensure proper relaxation of newly created chains. This stepwise increase in reaction cutoffs facilitates the timely generation of highly-crosslinked configurations by not only providing necessary post-reaction equilibration periods but also speeding up the remaining feasible reactions as the full reaction cutoff is reached. The different types of crosslink bonds that can be created in our simulations using the oligomer architecture in this study are depicted in figure 2(c) for reference.

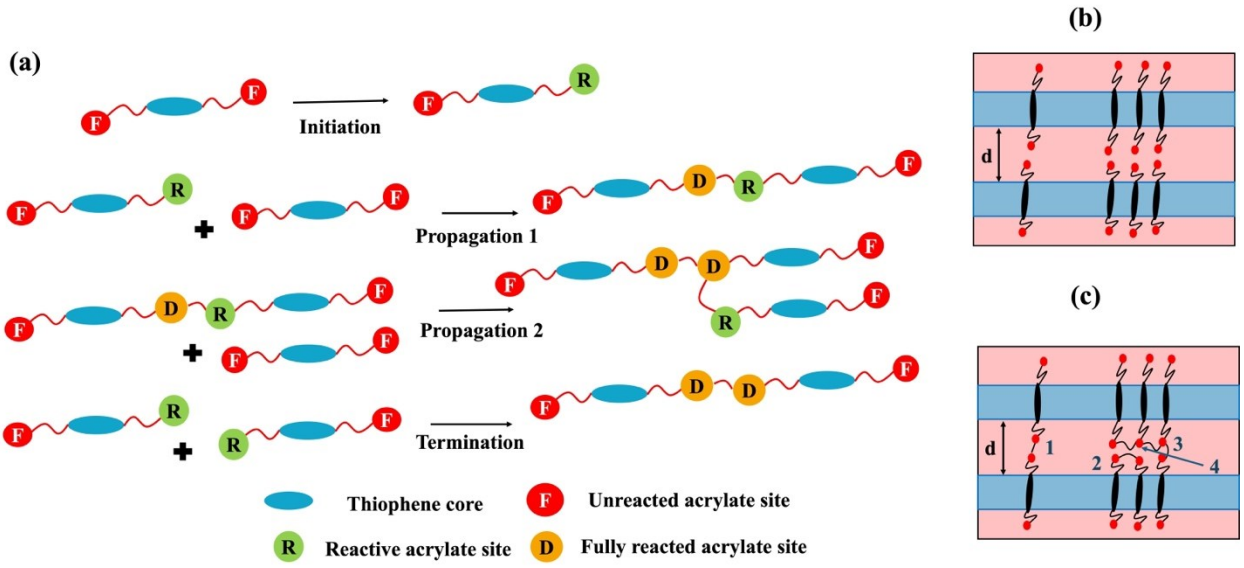

Figure 2. Schematics of crosslinking process. (a) The different reactions involved in the protocol. (b) Assembled configuration before crosslinking, where the black ellipsoids represent the thiophene cores, the curved lines represent the flexible chains, and the red dots highlight the acrylate functional groups. (c) Different types of changes in chain interconnectivity due to the crosslinking reactions, with acrylate functional groups involved in: (1) single inter-layer bond, (2) single intra-layer bond, (3) one intra-layer and one inter-layer bonds, and (4) two intra-layer bonds.

An experimentally relevant metric to characterize the progress of our crosslinking simulations is the degree of conversion, defined as:

$$DC\ \% = 100 \text{ x } (1 - M/M_0) \quad (4)$$

where, M = number of 'F' type beads left in the system after the crosslinking simulations, M_0 = total number of acrylate sites originally present ($M_0 = 2 \text{ x } N_{olig} = 8000$).

2.4. Deformation protocol

We used LAMMPS to perform uniaxial tension deformation simulations in the direction of lamella stacking (z in this study) for all systems in this study. We also adapt a similar protocol for performing detensioning simulations to characterize hysteresis behavior in these systems. The tensile deformation simulations were performed in a $N\sigma_x\sigma_y l_z T$ ensemble, where the box was deformed continuously at a fixed strain rate in the z direction while the normal stresses in x and y directions were fixed at 1 atm. This non-equilibrium MD (NEMD) deformation protocol allows for a continuous linear change in the box z dimension as, $l_z(t) = l_0(1 + \dot{\gamma}t)$, where l_0 is the initial z box length and $\dot{\gamma}$ is the imposed strain rate. Deformation in a constant lateral pressure ensemble also allows for a more natural pathway for the system to relax under the tensile strain imposed. Note that while performing the tensile deformations in a constant volume ensemble would enforce a system's Poisson's ratio of 0.5, this is not optimal for layered materials with varying levels of rigidity in the layers. For example, it has been shown that for lamellar block copolymer materials with glassy and rubbery layers, there is a significant drop in Poisson's ratio after the buckling instability develops.[42] The z strain value is calculated as, $\alpha = (l_z - l_0)/l_0$ and the normal stress response is found as, $\sigma_z = -P_{zz}$. To understand the effect of strain rate on deformation behavior (see section 3.4), four different strain rates spanning 4 orders of magnitude were used: $\dot{\gamma} = 5 \times 10^8$, $5 \times 10^7, 5 \times 10^6,$ and 5×10^5 s^{-1}. All NEMD simulations were performed at 300K using the Nose-Hoover thermostat and barostat with the corresponding damping parameters set at 100 and 1000 time steps respectively. Following earlier works simulating chemical reactions[43] and shape-memory thermo-mechanical behavior[44] with coarse grained models, the timestep was set at 10 fs for all simulations in this study. For characterizing the alignment of thiophene cores, the order parameter P_2 was used, which can be calculated as:

$$\langle P_2 \rangle = \frac{3}{2}\langle cos^2\theta \rangle - \frac{1}{2} \quad (5)$$

where θ is the angle between the end-to-end vector associated with the thiophene core (type 'T') beads of each molecule and the deformation direction (z axis). Characterization of local and global translational order was done using Steinhardt bond orientation order parameters,[45] which can be defined as:

$$Q_l = \left[\frac{4\pi}{2l+1}\sum_{-l}^{l}\left|\overline{Q}_{lm}(\vec{r})\right|^2\right]^{1/2} \quad (6)$$

Where, $\overline{Q}_{lm}(\vec{r})$ is the average complex bond vector given by:

$$\overline{Q}_{lm}(\vec{r}) = \frac{1}{N_b}\sum_{N_b}\overline{Y}_{lm}(\vec{r}) \quad (7)$$

where, $\overline{Y}_{lm}(\vec{r})$ is the spherical harmonics calculated for each bond vector, with the angles for each bond vector (θ, ϕ) defined with respect to an arbitrary reference frame. The local bond OPs are calculated as:

$$\overline{q}_l(i) = \left[\frac{4\pi}{2l+1}\sum_{-l}^{l}\left|\overline{q}_{lm}(i)\right|^2\right]^{1/2} \quad (8)$$

where the locally averaged bond vector can be calculated as:

$$\overline{q}_{lm}(i) = \frac{1}{N_b(i)}\sum_{k=0}^{N_b(i)} q_{lm}(k) \quad (9)$$

with $N_b(i)$ representing the number of neighbors for each bead i and $q_{lm}(k)$ representing the complex bond vector joining bead i and its neighbor k. We chose l = 6 in Eqs. (6)-(9) as Q_6 has been found to be a robust, rotationally invariant metric of crystallinity regardless of lattice geometry. Note that we adapted these calculations to describe the order around the inner thiophene

beads only; further details of the implementation and validation of these OPs can be found in section S14 of the SI.

3. RESULTS

3.1. Crosslinking

We first checked the robustness of our crosslinking protocol for ensuring reproducible results. From figure S2, it can be inferred that most of the crosslinking events occur for a reaction distance cutoff of 3.9 Å and 4.1 Å, which is similar to the van der Waals radius for the CG beads involved in the propagation and termination reactions ($\sigma = 4.28$ Å). We see a negligible increase in new crosslinking bonds formed after a cutoff of 4.7 Å, which suggests that the crosslinking process has converged and the final crosslinked configuration can be used for mechanical characterization studies. Also note that the final number of crosslinking bonds formed largely depends on the number of acrylate sites that we initiate before the crosslinking process, which is also reflected in the strong correlation between DC% and % initiation, as shown in Table 1. These statistics are collected over 5 different crosslinking reaction simulations, starting from the same assembled configuration at 300K. In Table 1, we also show statistics of the two classes of bonds formed in our crosslinking reactions: intra-layer and inter-layer, based on whether the bonds are formed between acrylate sites whose corresponding oligomer chains initially belonged to the same or adjacent thiophene layers respectively (in Fig. 2c, sites 1 and 2 are involved in a single interlayer and intralayer bond respectively). The number of bonds has been normalized by the initial number of oligomers present ($N_{olig} = 4000$) to provide a system-size independent metric. It is anticipated that these two classes of bonds formed play different roles in the tensile behavior of the system, with the inter-layer bonds being key in explaining the toughness trends observed in the system (see section 3.3). The statistics do show a similar composition of inter-layer (~ 42-43%) and intra-layer (~58%) bonds irrespective of % initiation. These statistics reflect the number of potential candidate bonds accessible to an acrylate site from the same/different layer. The higher fraction of intra-layer bonds suggests that the probability of an acrylate site encountering another acrylate site is higher within the same layer than from the adjacent layer. The fraction of initiated sites primarily controls the extent of crosslinking (total number of bonds formed at the end of the crosslinking period) but

has minimal effect on the relative proportions of potential bond types, hence leading to a nearly unchanging fraction of inter/intra layer bonds.

Table 1. Statistics for relevant crosslinking metrics with different % initiation

System #	% initiation	Degree of conversion (DC %)	N_{intra}/N_{olig}	N_{inter}/N_{olig}
1	10	19.1 ± 0.09	0.157 ± 0.005	0.114 ± 0.001
2	20	36.5 ± 0.21	0.29 ± 0.009	0.22 ± 0.005
3	30	51.9 ± 0.3	0.41 ± 0.005	0.31 ± 0.006
4	50	77.3 ± 0.35	0.583 ± 0.01	0.44 ± 0.012

3.2. Stress strain profiles.

3.2.1. Lamella breakage through buckling in uncrosslinked system

We first analyze the tensile response in the uncrosslinked system. Figure 3(d) shows the stress strain behavior at T = 300K for a strain rate, $\dot{\gamma} = 5 \times 10^6/\text{s}$. Initially, the system undergoes an elastic deformation until $\alpha \sim 0.1$, where the chain stretching occurs in both the rigid and the flexible regions, maintaining the original four-layer morphology, as shown in figure 3(a). Beyond this point, a buckling instability ensues, wherein the lamella tilts to form a 'chevron' morphology to maintain the domain spacing of the flexible regions. This deformation mode has been observed for smectic liquid crystals[46] and lamella forming glassy-rubbery block copolymer systems.[47,48] Using MD simulations for uniaxial deformation, it has also been shown that the apparent Poisson's ratio of the material deviates from the elastic limit, which has been explained by the concentration of the tensile deformation in the rubbery phase.[42] This deviation of Poisson's ratio due to buckling also justifies the use of a constant lateral-pressure ensemble instead of a constant volume ensemble for our tensile deformation studies.

For our system, we have two different types of layers – 'solid-like' layers comprised of the thiophene cores and 'liquid-like' layers made up of the flexible segments, as has been previously characterized in previous studies.[28] The thiophene cores pack aligned in the solid layer with their centers of mass forming a hexagonal lattice. According to the Poisson effect, if we stretch

(compress) the material along a certain direction (say along z axis), a tendency to compress (extend) is expected to occur in the other directions (i.e., x and y directions). This effect should affect all layers equally as a constant lateral pressure is maintained (0.1MPa) which precludes any pressure gradient. However, the natural response of the system to laterally compress is higher in the 'liquid-like' layers than in the 'solid-like' layers, where the hexagonal lattice would need to be deformed to undergo contraction. Hence, to maintain the domain spacing, the 'solid-like' layers adopt a "chevron" morphology, as shown in figure 3(b). This helps to relieve the extra uniaxial stress developed during the system's extension in the elastic regime, as confirmed by the significant drop in stress in the buckling regime in figure 3(d). With increasing strain, the chevron angles become sharper and the packing frustration of the chains around the tips of the "chevron" becomes energetically unfavourable. After $\alpha \sim 0.4$, the lamella breaks apart to relieve this packing frustration, forming 'islands' of lamella segments with their own local orientations, as shown in figure 3(c) and movie S1.

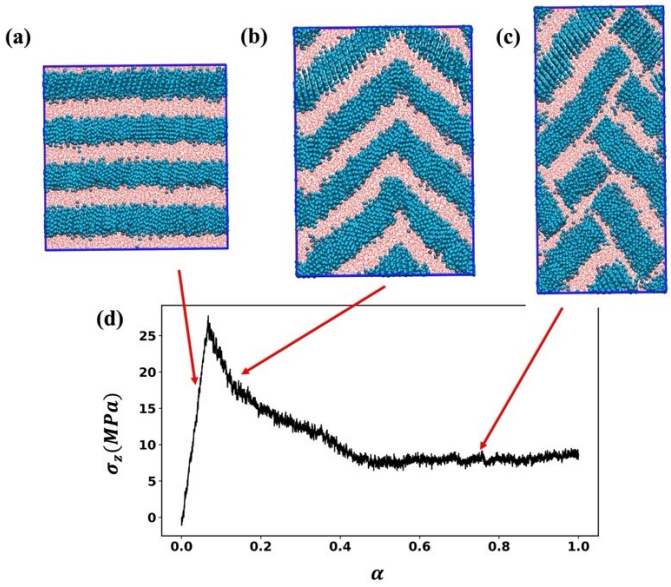

Figure 3. Tensile response of the uncrosslinked system. Simulation snapshots at different deformation regimes: (a) elastic, (b) buckling, (c) lamella breaking. Cyan = rigid thiophene core, red = flexible blocks comprising ethylene oxide (EO) units and acrylate sites. **(d)** Stress-strain profile.

3.2.2. Inter layer crosslinking facilitates layer re-crystallization transition

For systems 1, 2, and 3, we observe a "sawtooth-like" shape in the stress-strain profile as shown in figure 4(f). To explain this behavior, we will use system 1 (DC ~ 20%) as a reference, with the stress-strain profile and the simulation snapshots presented in figure 4. An example deformation simulation movie for system 1 is also provided in supporting information (movie S2). The corresponding figures for system 2 and 3 are shown in figure S4 of the Supplementary Material. We also performed deformation simulations starting from independently prepared system 1 configurations and obtained similar trends, as shown in figure S3, confirming the reproducibility of the tensile behavior. Initially, the deformation is elastic in nature, as reflected by the linear relation between stress and strain, and the initial four-layer morphology is maintained, as shown in figure 4(a). The primary difference between this and the uncrosslinked system is the presence of crosslinking covalent bonds connecting the layers, which causes stiffening of the 'liquid-like' layers to produce an increased Young's modulus in the elastic regime up to the yield stress point.

After a strain value of around 0.1, the buckling instability is again observed, as shown in figure 4(b). But in contrast to the uncrosslinked system, the stress does not monotonically drop to a significantly low value (~7 MPa) through buckling. At around $\alpha \sim 0.42$, the layered morphology is re-established as shown by the five-layer morphology in figure 4(c). This phenomenon can be attributed to the tendency of the rigid thiophene cores to recrystallize to maintain their equilibrium (most favorable) lattice spacing, and of the flexible blocks to maintain their equilibrium domain spacing. This "quasi-equilibrium" state, where the system attains a five-layer morphology is also associated with a local minimum in the stress-strain profile ($\alpha \sim 0.42$), as the recrystallization of thiophene to reform the lamella minimizes the free energy of the system, by lowering the interfacial energy between the rigid and flexible blocks and maintaining the favorable energetic contacts and packing entropy of the thiophene cores. A more detailed explanation of the events at the individual chain level that lead to this recrystallization behavior is provided in section 3.3. Upon further stretching, the system then responds in an "elastic-like" manner until α ~ 0.55, where the system

starts to undergo buckling deformation again, as shown in figure 4(d). The system eventually regains the layered configuration, with a transition to a six-layer morphology occurring at $\alpha \sim 0.7$. This tensile behavior is reminiscent of that of some materials with shape-memory and self-healing properties as the system tends to 'remember' its initial morphology throughout the tensile response while avoiding reaching high bond-breaking stresses.

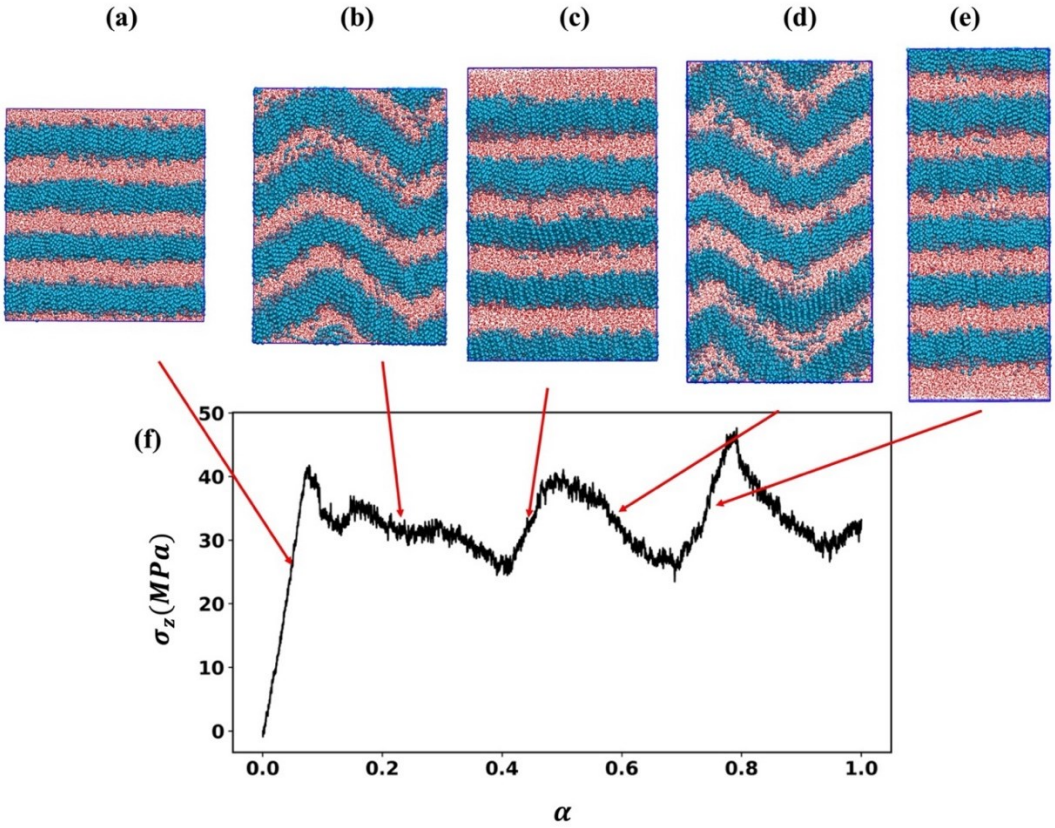

Figure 4. Tensile response of crosslinked system 1. Simulation snapshots at different regimes; elastic (-like): (a), (c), and (e) and Chevron (b) and (d). Cyan = rigid thiophene core, red = flexible blocks comprising ethylene oxide (EO) units and acrylate groups. (f) Stress-strain profile.

3.2.3. Layer recrystallization is hindered in highly crosslinked systems

For system 4, the stress-strain profile is qualitatively different from the partially crosslinked systems. In the elastic regime, we expectedly see a higher modulus than in systems 1, 2 and 3, as the highly connected network topology created in system 4 makes the initially plastic 'liquid-like' layers to be fully elastic. As shown in figure 5, after the elastic regime, we see a stress plateau until

$\alpha \sim 0.5$. This regime is commonly associated with the 'soft-elasticity' behavior as described in theoretical and experimental studies of LCEs.[10] The stress plateau implies that the excess force being applied to stretch the system is absorbed to cause topological changes in the crosslinked network from their original layered morphology. Between $\alpha \sim 0.5$ and 0.7, there is a small shoulder in the stress-strain profile, which coincides with a weak reordering of lamella with diffuse interface between rigid and flexible layers, as shown in figure 5(c). The reordering is further confirmed by performing an additional NPT-ensemble equilibration period using a starting configuration from $\alpha = 0.6$, which allows the system to relax any strain-induced internal stresses. A representative simulation snapshot of the resulting near-equilibrium state is provided in figure S11(g), which shows a similar recrystallization tendency of the thiophene cores as explained in section 3.2.2. However, unlike system 1, this tendency is reduced due to longer intrinsic relaxation times and higher topological constraints of the chains, a direct consequence of the highly connected network-like structure, which leads to a weaker reordering of the lamella. Beyond $\alpha \sim 0.7$, the stress increases monotonically, which implies that the chains in the flexible segments are getting increasingly stretched and there is no room for collective rearrangements that could allow 'absorption' or reallocation of the input stretching energy. At such high strain, we do not observe reformation of lamella either (as seen in movie S3), unlike the case of the partially crosslinked systems discussed in section 3.2.2. Note that after the elastic regime the thiophene cores are predominantly aligned with respect to the deformation direction (z) as indicated by the P_2 trend in figure 5, consistent with nematic order in the system. These observations indicate that beyond $\alpha \sim 0.7$, the system loses its original global translational order but maintains orientational order, behaving like a more typical nematic elastomer. The loss of global translational order is further validated by a decrease in the global Q_6 beyond $\alpha \sim 0.7$, which is a result of a decrease in thiophene core packing density and fraction of beads with local solid-like character. The former is confirmed by the decrease in the RDF peak intensity in figure S14 (c) and the latter by a broader, more heterogeneous distribution of local $\overline{q}_6$ values in figure S17(c).

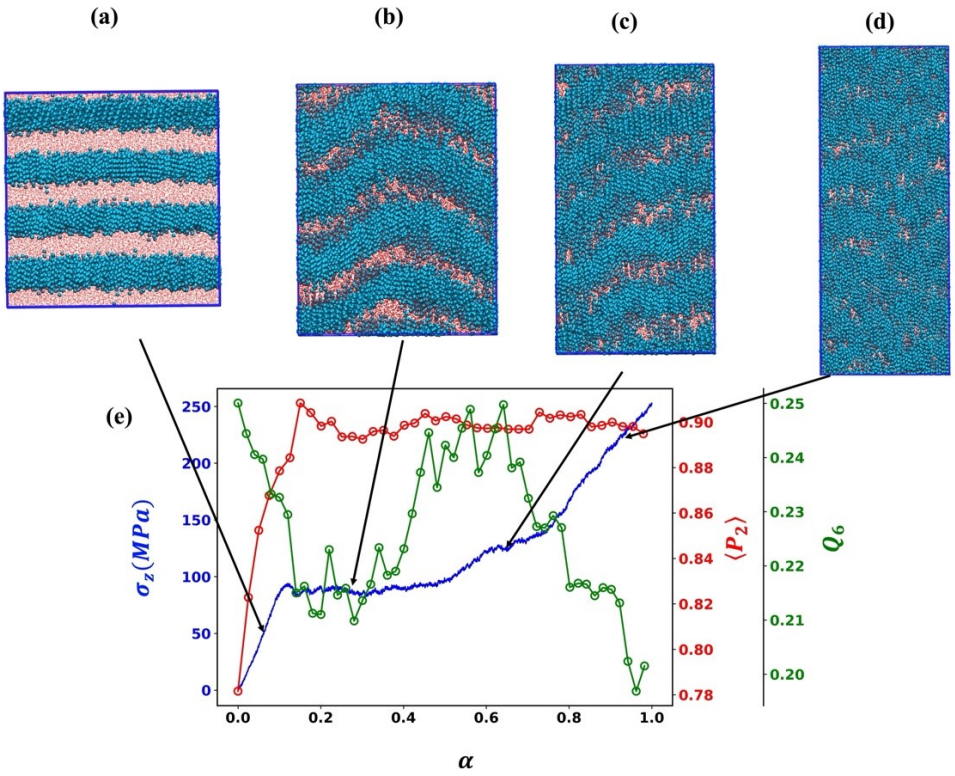

Figure 5. Tensile response of crosslinked system 4. Simulation snapshots at different regimes; elastic (a), chevron (b), diffuse-layered (c), highly stretched (d). Cyan = rigid thiophene core, red = flexible blocks comprising ethylene oxide (EO) units and acrylate groups. (e) Stress-strain (blue) and order parameters P_2 (red), global Q_6 (green) profiles.

3.3. Thiophene alignment though interlayer coupling promotes layering transition

In this section, we put forward an explanation for the layer transition behavior in the partially crosslinked systems, based on the behavior of the P_2 order parameter for the thiophene cores in the system. The P_2 trends are plotted with the stress strain profile for the uncrosslinked and system 1 (DC ~ 20%) in figure 6(a) and 6(b) respectively.

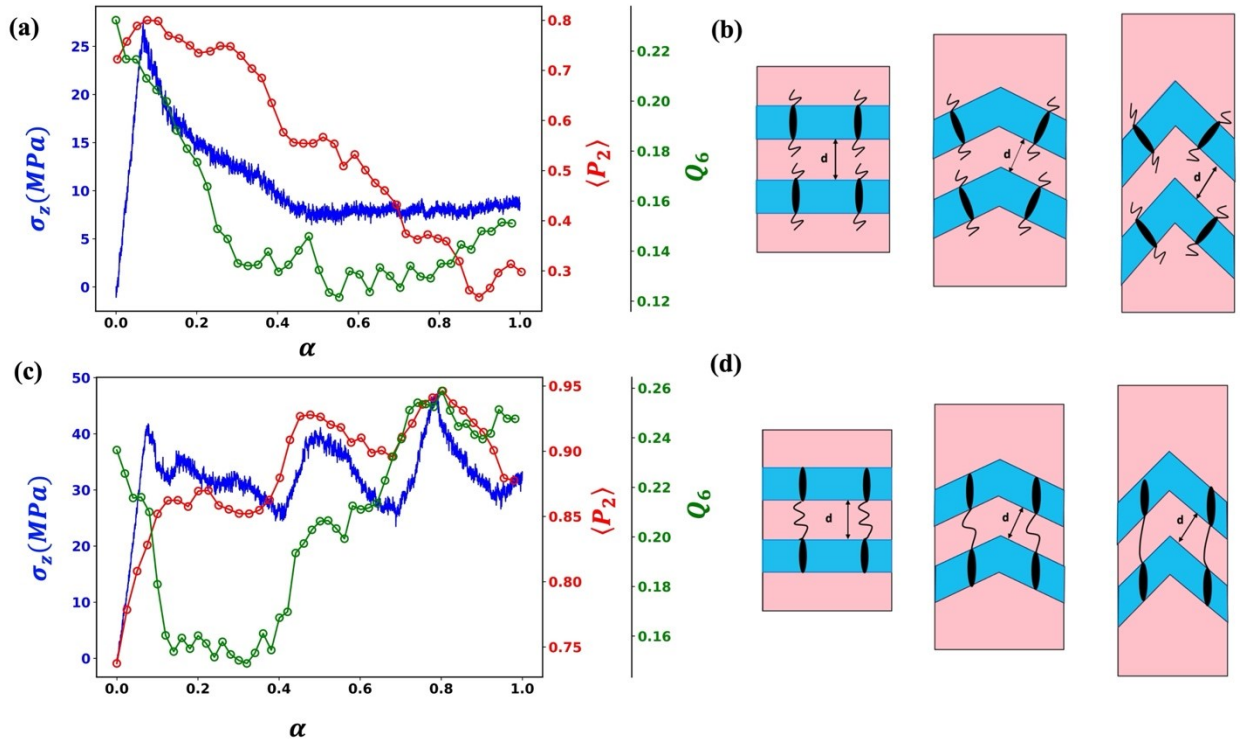

Figure 6. Trends of stress (blue) and order parameters P_2 (red), global Q_6 (green) vs. strain for uncrosslinked (a) and crosslinked system 1 (c)**.** (b,d) Schematic showing chain-level behavior as the "chevron" deformation mode becomes sharper with strain for uncrosslinked (b) and partially crosslinked system (d). The cyan and light-pink regions represent the rigid and flexible layers in the system, with the ellipsoids depicting the thiophene core and the curvy lines depicting the flexible segment. For the crosslinked system, only two examples of flexible chains resulting from inter-layer crosslinking are shown.

In the initial elastic regime (up to $\alpha \sim 0.1$), we see a small rise in P_2 for both the uncrosslinked and partially crosslinked systems, indicating an increase in the alignment of the thiophene cores along the tensile strain direction (z). This likely stems from the alignment of some misaligned thiophene cores in the original layers. During the buckling regime, we see a consistent drop in P_2 for the uncrosslinked system, from 0.85 at $\alpha \sim 0.1$ to 0.6 at $\alpha \sim 0.4$, where the lamella starts to break and form 'islands'. During this regime, the best way for the thiophene cores to maintain the hexagonal packing locally is to tilt with the lamella, as shown in figure 6(b), which is consistent with the drop in P_2. After the lamella breaks, there is a further drop in P_2 with strain, which indicates that each of these broken lamella fragments can maintain the ordered packing of thiophene cores

independent of other fragments. The director vectors for these broken fragments also gradually decouple, leading to a steady drop in the global P_2 as tensile strain increases.

For the partially crosslinked system, there is a very small drop in P_2 (from 0.875 to 0.85) as the buckling deformation proceeds. This indicates that the thiophene cores tend to remain aligned along the deformation axis during the buckling regime(s), which is also portrayed in figure 4(d). To explain the schematic in figure 6(d), let's consider a simple case of two thiophene cores, initially present in adjacent layers, which are connected to each other due to inter-layer crosslinking. In contrast to the uncrosslinked system, as the "chevron" morphology sharpens during buckling, the thiophene cores coupled across two layers cannot freely tilt as it would require concerted changes to their lattice structures in both layers. Similarly, they cannot laterally displace within their layers, as this would generate high lattice stresses to their 'solid-like' arrangements. Given the preferential alignment of the thiophene cores along the deformation direction, the flexible chains connecting the cores must stretch to maintain the domain spacing of the flexible layer. Thus, even when the global stress in the system reduces, there is an increase in the total potential energy in the system, and a reduction in the conformational entropy of the flexible chain, both of which are unfavorable to the system's free energy. To counteract such penalties, some clusters of thiophene cores detach from their current layer and recombine with adjacent layers to reform the lamella morphology. This redistribution of chain domains, shown in movie S5, is facilitated by the mobility of the sparse crosslinking sites which join the thiophene cores from the adjacent layers. This chain redistribution is absent in the uncrosslinked system, as can be seen in movie S4, which suggests that in that case the cooperative motion of the oligomer chains is constrained to occur only within each single layer. On the other hand, the fact that we only observe a diffuse layer-transition behavior in system 4, where the thiophene cores are dispersed throughout the system, suggests that the mobility in the 'liquid-like' domains is significantly reduced due to the dense crosslinking at DC ~ 80%. This reduced mobility can be seen in figure S12(a), where we compare the average mobilities of the crosslink sites for the uncrosslinked case and systems 1 and 4. Thus, for the layer-transition behavior to occur, there needs to be a balance between interlayer coupling and sufficient plasticity in the flexible layers, the latter being manifested by a higher average mobility of the crosslinking sites.

The stress-strain recrystallization behavior can be further correlated with the global trends of the Q_6 order parameter (associated with inner thiophene beads only) for the uncrosslinked system (figure 6a) and system 1 (figure 6c). Details of the implementation and a Q_6-value calibration for a reference system are provided in section S13 of the SI. For both systems, in the elastic regime we see a slight drop in the global Q_6 even as the thiophene cores get more aligned along z and the layering is maintained, which can be associated with the cores getting displaced out of their equilibrium positions and creating a more diffuse Thiophene-EO interface. In the buckling regime, we see a drop in global Q_6 for both systems, which reflect a decorrelation of the bond vectors due to the 'chevron' pattern formation. For the uncrosslinked system, upon lamellar breakage, the global Q_6 remains constant as the bond vectors in each lamellar 'island' remain correlated, albeit decorrelated from the other 'islands'. This is supported by the fact that the local $\overline{q}_6$ distribution (figure S17a) is largely maintained throughout the strain range, indicating that the initial local crystallinity is conserved. For system 1, the initiation of layer reformation events (through the mechanisms discussed earlier) occur with a concurrent rise of Q_6. This suggests that the bond vectors around inner thiophene beads, which had lost some correlation in the buckling regime, realign as the crystal-like layers reform, signaling the 'recrystallization' events seen in the simulation stress-strain profiles and snapshots. Subsequent layer reformation events in system 1 (for $\alpha > 0.5$) do not significantly reduce Q_6, a behavior likely correlated with the ensuing higher alignment of thiophene cores (reflected by high P_2 values).

3.4 Energetic and conformational effects on stress response

To evaluate the energetic and entropic contributions to the tensile response for the crosslinked systems, we tracked different contributions to the potential energy and the end-to-end distance distributions of the (original) chains as a function of strain. As discussed in Section S14 of the SI, different components of the potential energy exhibit variations that tend to be correlated (in non-trivial ways) with the ups and downs of the stress-strain profiles. Here we only report on the energy arising from thiophene-thiophene non-bonded interactions (ΔU) as a representative metric expected to correlate with recrystallization. The chain end-to-end distance (R_{ee}^*) distributions can capture conformational stretching and contraction trends of the chains, and hence we devised a

metric $\langle|\Delta P|\rangle$ that quantifies their deviation from the reference, most relaxed unstrained ($\alpha = 0$) state:

$$\langle|\Delta P(\alpha)|\rangle = \frac{1}{N_{bins}}\sum_{i\in N_{bins}}|P(i;\alpha) - P(i;0)| \tag{10}$$

where, $P(i;\alpha)$ is the probability density of the R_{ee}^{*} value (corresponding to the histogram's i^{th} bin) for strain α. This mean absolute deviation reflects conformational entropic penalties associated with chain deformations. Figure 7(a) shows results for ΔU and $\langle|\Delta P|\rangle$ for system 1, illustrating that the recrystallization behavior is correlated with changes in energetic interactions (i.e., stress drops tend to align with lower, more favorable thiophene-thiophene interactions), while the conformational penalty is largely constant for the strains probed beyond the elastic regime. However, for system 4 in figure 7(b), both energetic and entropic penalties contribute to the upturn in stress at high strains.

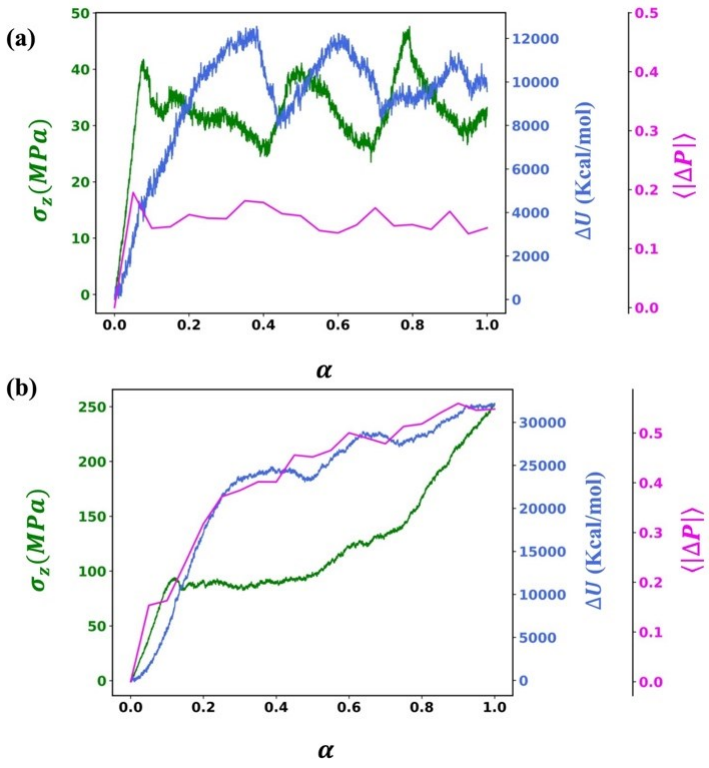

Figure 7. Variation in representative energetic (ΔU) and entropic ($\langle|\Delta P|\rangle$ metrics along the stress profile for (a) system 1 (DC ~ 20%), (b) system 4 (DC ~ 80%)

3.5. Effect of strain rate

Tensile responses are generally strain-rate dependent, with our simulations needing to operate at very high rates for computational tractability. This dependence arises from the competition of the deformation time scale and the different relaxation time scales within the material (i.e., for the faster local rearrangements and the slower multimolecular cooperative re-crystallization). Note that slower rates are more realistic and allow the stress response to approach the conditions for quasi-equilibrium deformation (corresponding to an infinitely slow strain rate). We thus attempted to quantify the effect of strain rates on the different tensile behaviors observed for the uncrosslinked, partially crosslinked, and highly crosslinked systems. For the uncrosslinked system, the qualitative behavior is the same across all the strain rates as shown in figure S9(a), likely reflecting the faster molecular relaxation mechanisms involved and suggesting that our results could be seen as being quasi-equilibrium responses. For the partially crosslinked system in figure 8, there is a noticeable qualitative difference in the response across the strain rates. For the faster $\dot{\gamma} = 5 \times 10^8\ \mathrm{s}^{-1}$ (stress-strain profile in figure S8) and $5 \times 10^7\ \mathrm{s}^{-1}$ rates, there is a consistent drop in stress after the elastic deformation regime without the sawtooth-like trends nor the associated recrystallization behavior described in section 3.2.2. This implies that the deformation mechanism is different from those for the slower $\dot{\gamma} = 5 \times 10^6\ \mathrm{s}^{-1}$ and $5 \times 10^5\ \mathrm{s}^{-1}$ rates, where we do observe a 'sawtooth-like response behavior. This crossover in deformation behavior suggests that the 'effective' time scale for chain redistribution in the system, estimated as reciprocal of the strain rate, is between $\tau \sim\ 20 - 200$ ns. The reproducibility of the sawtooth-like behavior for $\dot{\gamma} = 5 \times 10^5\ \mathrm{s}^{-1}$ also supports the mechanism proposed in section 3.3, as with a slower strain rate, the crosslinked chains get more time to relax and detach from their current layers as described in section 3.3. This allows the thiophene cores to timely recrystallize and the sawtooth-like tensile response to emerge. Note, however, that the coarse-grained nature of the model implies that some scaling factor would be needed to calibrate the time scales and hence any analysis of dynamics is more meaningful in considering (relative) values and trends.

For the highly crosslinked systems, beyond the elastic regime, there is a stress plateau followed by strain hardening for all the strain rates (see results in figure S9), as explained in section 3.2.3. The slower relaxation of the highly crosslinked network is a likely contributor to the limited recrystallization in these systems for all strain rates studied. However, a proper quantification of this effect would require performing tensile simulations at extremely low strain rates (say 4-5 orders of magnitude slower) which are currently computationally unfeasible.

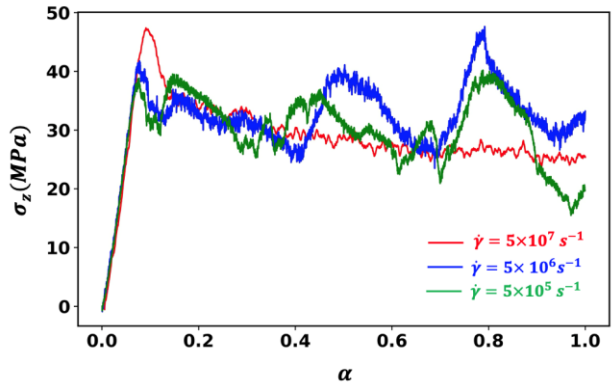

Figure 8. Stress-strain profiles for system 1 with different strain rates. Red, blue, and green curves represent strain rates $\dot{\gamma} = 5 \times 10^{7}\ \mathrm{s}^{-1}, 5 \times 10^{6}\ \mathrm{s}^{-1}$ and $5 \times 10^{5}\ \mathrm{s}^{-1}$ respectively.

3.6. Hysteresis trends

3.6.1. Strain hysteresis

One question that arises from the stress-strain profile of systems 1 or 4 is whether upon unloading the system from a strained state, it reverts back to the original four-layer state at zero strain. To answer this question and characterize the hysteresis in the stress-strain behavior, we perform contraction simulation in the $N\sigma_x\sigma_y l_z T$ ensemble, starting with a configuration at a selected strain value of interest. The deformation rates for these simulations can be interpreted as 'destraining' rates and are adjusted based on the original unstrained length to maintain the same extent of deformation per timestep. In this section, we use the uncrosslinked system and system 1 (DC ~ 20%) to examine the effect of crosslinking on hysteresis behavior. We choose strain values of $\alpha = 0.2, 0.6$, which represent different regimes in the stress-strain profile for both systems, as explained in section 3.2. We observe qualitatively similar hysteresis trends for $\alpha = 0.2$ case for both systems,

where the system regains the four-layer lamellar configuration from the buckled four-layer state, as shown in figures 9(d) and 10(d). The system stress also approaches zero at the end of the contraction simulations, indicating a qualitative similarity of this end state to the initial unstrained state.

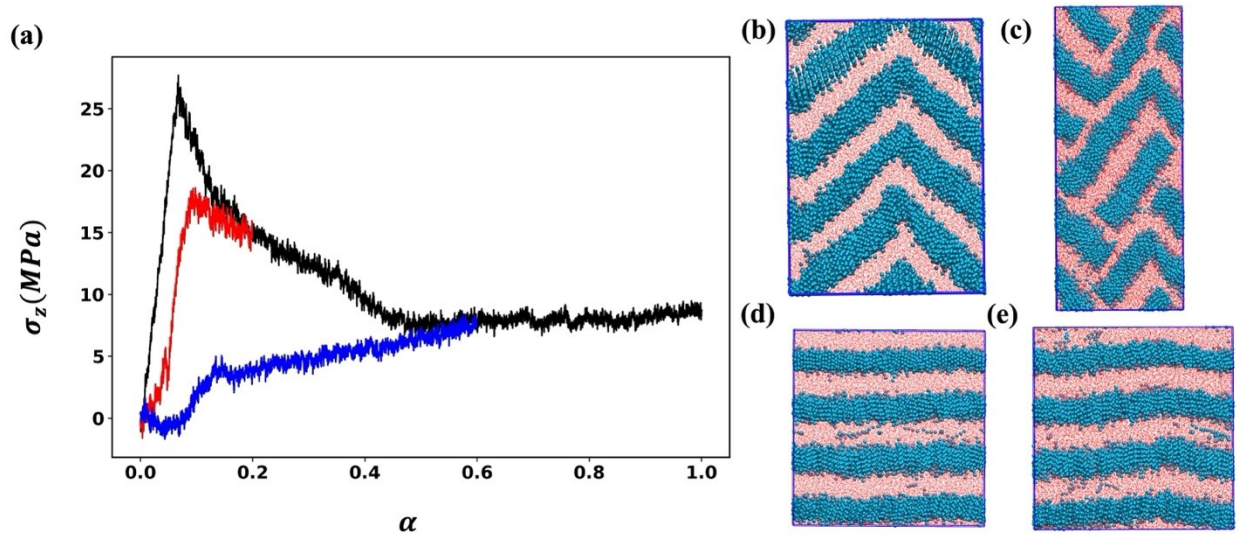

Figure 9. (a) Hysteresis in stress-strain profile for uncrosslinked system. Black curve represents the tensile deformation described in section 3.2.1, red and blue curves represent contraction deformations from $\alpha = 0.2$ and 0.6 respectively. (b)/(d) shows the initial/final configuration for contraction from $\alpha = 0.2$, and (c)/(e) shows the initial/final configuration for $\alpha = 0.6$.

For the $\alpha = 0.6$ case with the uncrosslinked system, we observe upon destraining that the system regains the original four-layer lamellar configuration from the 'broken lamella' state with the system stress returning to zero. However, for system 1 in Fig 10 (where the $\alpha = 0.6$ corresponds to a *Chevron* five-layer state), the system stays trapped in a five-layer morphology, with a finite (non-zero) stress at zero strain, which likely results from the suboptimal structure which generates a residual stress from the frustrated tendency of the system to conform to the four-layer box dimensions. Indeed, upon destraining the system from $\alpha = 0.6$, the stress drops to zero at similar strain value ($\alpha \sim 0.42$) where the five layer is formed upon tensile deformation (see section 3.2.2). Upon further destraining, a compressive stress (hence the negative values) develops in the system, which indicates that the five-layer morphology is not an ideal fit the box dimensions at such strains,

and there remains a tendency for the system to rearrange to box dimensions compatible with four layers. In general, if contraction is allowed from a strained state α_x, the final zero strain state can be predicted to have a number of layers commensurate with a z box size slightly lower than α_x. This is also consistent with the hysteresis trends in system 4 (figure S10), where the system tries to regain a lamellar morphology from $\alpha = 0.6$ and 1.0, but the simulation snapshots at zero strain, figure S10 (f) and (g) respectively, reveal that such a microphase segregation is frustrated resulting in diffuse interfaces between the thiophene and ethylene oxide blocks.

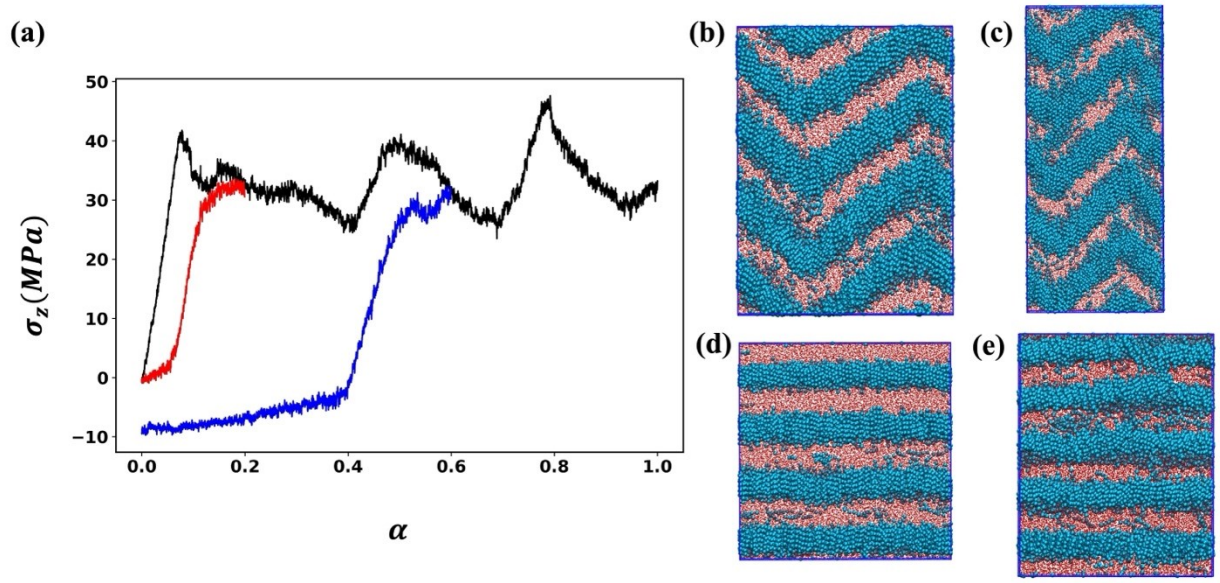

Figure 10. (a) Hysteresis in stress-strain profile for system 1 (DC ~ 20%). Black curve represents the tensile deformation described in section 3.2.1., red and blue curves represent contraction deformations from $\alpha = 0.2$ and 0.6 respectively. (b)/(d) and (c)/(e) represent the initial/final configurations for contraction from $\alpha = 0.2$ and 0.6 respectively.

3.6.2. DC% modulates memory retention

For crosslinked systems, it can be argued that the degree of conversion (DC) acts as a surrogate metric to assess the tendency of the system to retain the original lamellar structure. One way to probe lamellar stability is by determining the upper temperature range over which the structure is stable. For this, we performed NPT ensemble simulations starting from different strained/unstrained states at temperatures ranging from 300 - 550K in increments of 10K to assess the apparent order-disorder-transition temperatures (T_{ODT}), with a higher T_{ODT} value indicating higher thermal stability. A comparison of the density (ρ) thermal dilation curves for various

unstrained states is provided in figure 11 for different DC, along with the original cooling T-ρ curve obtained from the assembly simulations detailed in section 2.1; discontinuities or inflexions along the given curve signal the ODT point or region. For the uncrosslinked system, we do see a considerable hysteresis between the heating and cooling cycles, with the cooling ODT being ~ 400K, while the heating ODT being ~ 430K. The ODT keeps increasing from 430K to 520K for lamellar configurations prepared with higher DC (up to 80%). This is likely due to the increased connectivity between the oligomer chains (due to inter or intra-layer crosslinking), which effectively increases the overall density of the system and reduces the propensity of the chains to disorder due to thermal fluctuations.

We observe similar T-ρ curves for heating simulations starting from a strained state (e.g., for α = 0.6 with system 1 in the inset of figure 11). Note that by performing NPT-ensemble equilibration runs starting from a strained state, we also release the external force the system was experiencing due to the tensile deformation (i.e., a constant pressure condition replaces a constant strain along the z-axis). Hence, this also allows us to address what happens if the tensile force is suddenly removed and the system is allowed to relax under ambient conditions. Representative equilibrated simulation snapshots for different systems at 300K are provided in figure S11. Starting from α = 0.2, which represents the buckled regime, all systems relaxed back to a four-layer morphology upon equilibration. Starting from α = 0.6, the uncrosslinked system retains the broken lamellar regime upon releasing the tensile strain. However, for system 1, starting from α = 0.6 where it has a five-layer buckled configuration (shown in figure 4d), it relaxes to a well-aligned five-layer configuration (lamellae stacked parallel to the original stacking z direction), shown in figure S11(d). This also suggests that upon releasing the applied strain, the system retains 'memory' of the original multi-layer stacking orientation and points toward the presence of a free-energy barrier between the four- and five-layer free-energy basins. This argument is also supported by the stress-strain profile we observe for system 1 (figure 4f). Indeed, when the system transitions from a four-layer buckled state to well-stacked five-layer structure (and for subsequent layering transitions), the stress does not drop to zero and instead, maintains an average stress consistently over a wide strain range, contributing to a higher toughness. For system 4, upon releasing the external tensile force, the diffused layer interfaces at α = 0.6, become sharper as seen in figure S11 (f), and hints at a partial recrystallization of thiophene cores during the tensile deformation as explained in section 3.2.3. At α = 0.8, where there is a general loss of translational order for system 4 during

the deformation and, upon releasing the stress, there is no observable restoration of a lamella structure, while there is a clear reordering for system 1, as seen in figures S11. From this discussion, it can be concluded that while higher DC helps in maintaining layered structure at higher temperatures and low strains, it can also hinder 'partial memory retention' at higher strains due to slower relaxation times of the networks formed due to crosslinking. Thus, for applications pertaining to memory retention and wider extensibility of the material, partial crosslinking would be preferrable.

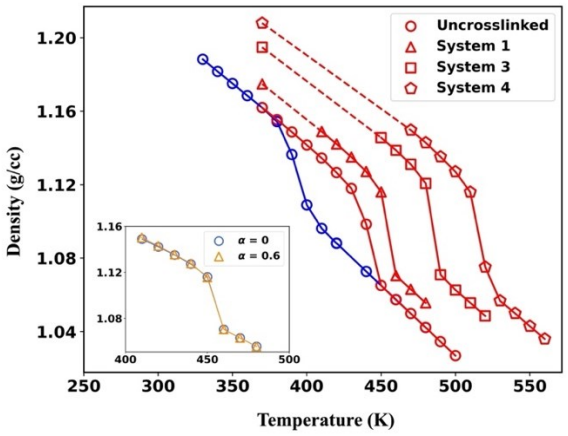

Figure 11. Temperature-density plots for all systems: Blue = cooling and red = heating curves. Inset shows the heating curves for system 1 starting from unstrained ($\alpha = 0$) and buckled five-layer state ($\alpha = 0.6$).

3.7. Alternate oligomer designs not requiring crosslinking.

The lessons learned on the effect of crosslinking on the tensile behavior of the 4T/dEO4 oligomer (which has an ABA block sequence) suggest that a similar effect could be attainable with alternate oligomer designs which intrinsically incorporate inter-layer coupling in the absence of crosslinking reactions. While avoiding the need for the crosslinking step could help simplify the processing needed to assemble the target structures (potentially facilitating experimental deployment), the oligomers should not be too large or complex as that would negate some of the favorable kinetic behavior associated with the faster assembly and defect annealing of smaller molecules. Accordingly, the alternate oligomer architecture we choose as representative of this approach is a

simple modification of the original triblock architecture, as it considers the case when two ABA molecules are joined at the one end, as shown in figure 12 (b). This new oligomer architecture, henceforth referred to as ABA2, primarily adopts two types of conformations when self-assembled into the lamella phase, namely 'looped and 'stretched', as shown in figure 12 (c) and (d) respectively. The coarse-grained bead types are the same as detailed in section 2.1 and the bonded and non-bonded parameters involving the different types of beads present in the system are the same as reported in tables S1-S3. To prepare a four-layer configuration, we consider 1600 molecules with the ABA2 architecture, and for the self-assembly, we use the same protocol (with the 'guiding' field) as reported in section 2.2.

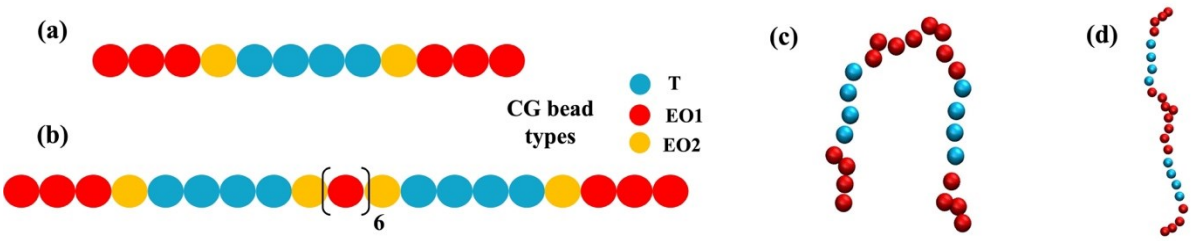

Figure 12. CG model representation with the different bead types for the original ABA (a) and ABA2 (b) oligomer architecture. Representative snapshots of the 'looped' (c) and 'stretched' (d) conformations

The tensile deformation simulations for this system were performed at $\dot{\gamma} = 5 \times 10^6\ s^{-1}$ using the same protocol as detailed in section 2.4. The stress-strain profile along with representative snapshot for different tensile regimes are provided in figure 13. The observed stress-strain response profile with its different tensile regimes is very similar to that of system 1 (shown in figure 4). The P_2 trends, shown in figure 13, are also qualitatively similar to those for system 1, indicating that the thiophene cores consistently tend to align with the deformation direction (z in this case). We also measure end-end distance of the oligomer chain along the deformation direction to see if there are morphological changes during the deformation. The inset of figure 13 (e) shows the distribution of the order parameter (OP), the end-end distances of the oligomers along the deformation direction (z), at the initial and final points of the deformation simulation. The general trend observed shows a bimodal distribution, with the first and second modes representing the 'looped' and 'stretched' configuration types respectively. There does not appear to be a major shift in the

two modes throughout the deformation, which indicates negligible looped-to-stretched configuration transitions during the deformation process. The small shift in the mean of the second mode arises from the stronger alignment of the 'stretched' chains along the deformation direction, resulting in higher OP values (as also reflected by slightly higher P_2 value at $\alpha = 1$). The reformation of the lamella during the tensile deformation is not expected for the ABA architecture shown in figure 12 (a), which can be anticipated to exhibit a stress-strain profile similar to the uncrosslinked system reported in section 3.2.1. The presence of the interlayer bonds due to the 'stretched' conformations, which is the key contrasting feature of the assembled configurations for ABA2 and ABA architectures, thus seems to serve a similar role as the inter-layer crosslinks in system 1, facilitating the recrystallization of the thiophene cores and the reformation of the lamellar morphology from the buckled states.

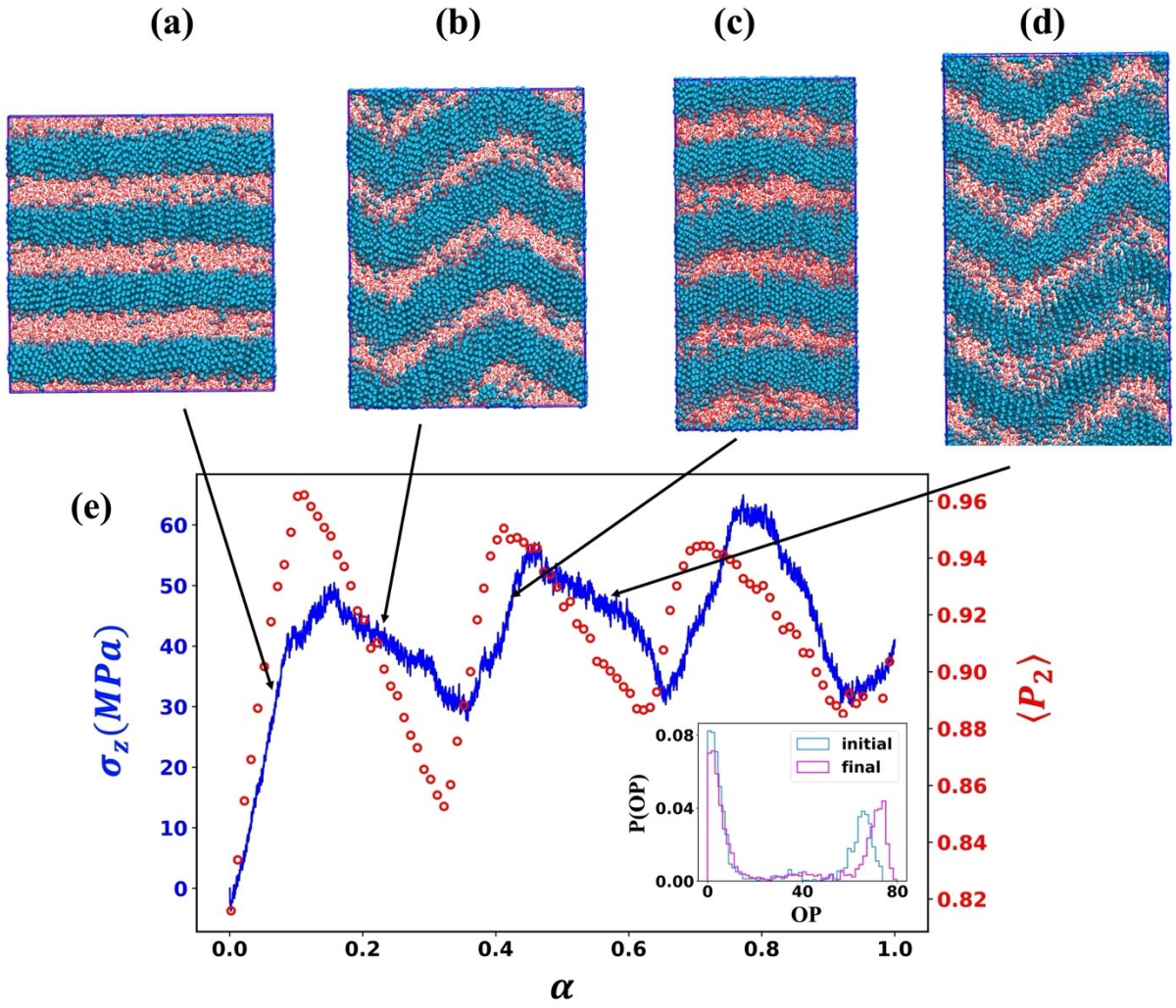

Figure 13. Tensile response of lamellar ABA2 system. Simulation snapshots at different regimes;

elastic (-like): (a), (c) and Chevron (b) and (d). Cyan = thiophene core, red = flexible blocks comprising ethylene oxide (EO) units and acrylate groups. (e) Combined stress-strain profile (blue) and P_2 trends (red). Inset shows probability density of the OP described in section 3.7 for the 'initial' ($\alpha = 0$) and 'final' ($\alpha = 1$) configurations of the deformation.

4. CONCLUSION

In this work, we observe a toughening behavior in a system of crosslinkable coil-rod-coil ABA oligomers pre-assembled into a lamellar phase and then crosslinked using a reaction protocol to emulate the UV based crosslinking reactions. Specifically, we observe 'sawtooth-like' profiles in the stress response for partially crosslinked systems subject to tensile deformation in the direction parallel to lamellar stacking, for strain rates $\dot{\gamma} = 5 \times 10^6\ \mathrm{s}^{-1}$and $5 \times 10^5\ \mathrm{s}^{-1}$. This originates from the recrystallization of the central 'rod-like' cores of the oligomers which we ascribe to the interlayer linking of thiophene cores that couples their alignment along the direction of deformation. During buckling regimes, this preferential alignment forces the chains connecting the 'solid-like' layers to stretch, as illustrated in Figure 6, creating internal stresses in the system. To minimize this penalty, the system tends to find a lamellar packing commensurate with the box dimensions at any given strain, which is attainable only if the extent of crosslinking is moderate. We also observed the sawtooth-like stress-strain profile for an uncrosslinked ABA2 oligomer design with the reformation of lamella, similar to that for ABA systems with partial crosslinking. This further supports that interlayer coupling, in the form of 'stretched' conformations in this case, promotes toughening and high extensibility, making the overall system be more solid-like while maintaining a balance of elastic and plastic features at the microscopic level.

The ABA uncrosslinked system did not exhibit a saw-tooth stress-strain profile or recrystallization of layers, instead, the original lamellar layers buckle and eventually break apart in response to the tensile deformation. The thiophene cores tilt along with the lamella during the buckling and the lack of 'connection' between the layers does not promote the recrystallization of the broken domains. For the highly crosslinked system, we observe an 'elastomer-like' stress-strain profile commonly observed in experiments with LCEs, where a stress plateau regime occurs after the elastic regime, followed by a weak reordering of thiophene cores with diffuse thiophene-ethylene oxide domain interfaces and eventually, a monotonous rise of the stress (which would

continue till failure). At such high levels of crosslinking the 'recrystallization' nearly disappears due to the lack of mobility of the numerous crosslink sites in the 'liquid-like' layers, which also causes the thiophene cores to align into a nematic morphology (lacking translational or layering order) at high strains. While this response is strain-rate dependent, it is unlikely that 'recrystallization' behavior will occur at lower strain rates than those used in this work given the highly entangled nature of the chains within the material.

For this study, we adopted a coarse-grained model developed for thiophene-ethylene oxide (EO) block based system, which incorporates the rigid nature of oligothiophenes due to $\pi - \pi$ stacking and the flexible nature of the ethylene oxide block. Previous studies have estimated the Flory's Chi parameter for the two blocks as $\chi_{4T-PEO4} \sim 0.007$,[31] indicating that block chemical incompatibility is not the main driving force for the lamellar phase formation, but rather is their difference in packing structures and melting points T_m (with $T_m > 300$ for the oligothiophene and $T_m < 300$ for the oligoethylene oxide). While the present model properly captures the main physical features of the constituent blocks, some structural details are missing, e.g., the thiophene cores do not pack in the experimental herringbone lattice. While such details may play a secondary role in our results, it would be appropriate to study finer grained models and even fully atomistic systems which would also allow more quantitative estimations of stress and toughness values.

On the other hand, the coarse-grained nature of our model implies that the results presented here are more generally applicable than to the specific chemistry used to construct this model. Indeed the "inverse" mapping of our CG model into a chemistry-specific system is non-unique in that many chemistries could be found that are consistent with it, i.e., as long as the main physical features of the model are matched, namely, the effective inter-block Chi parameter, the relative block contour lengths and their persistence lengths (or backbone stiffnesses).

The results for the tensile deformation simulations show that the toughening behavior originates in the crystallizable nature of the rigid thiophene cores. It will be interesting to explore the interplay of the backbone rigidity and the block incompatibility (χ_{eff}) (both of which can independently drive the formation of lamellar morphologies) on the layering transitions and toughening behavior observed in this type of system. Having a lamellar morphology with high χ_{eff} could hinder the recrystallization as it involves the transient mixing of the two blocks through redistribution of thiophene cores across adjacent layers, as shown in movie S5. However, increase in block incompatibility has been seen to increase toughness of model diamond networks of ABA block

copolymers.[23] On the other hand, reducing the backbone rigidity could negatively impact the recrystallization behavior by reducing the tendency of the chains to preferentially align along the deformation direction. In terms of molecular architectures, controlling the lengths of the thiophene and EO blocks (hence, the $\chi_{eff}N$ and/or the block volume fractions) could help enlarge the 'teeth-like' stress profile observed here, hence enhancing toughness. Finally, it would be informative to explore the response of this class of materials to different types of deformation, e.g., by performing uniaxial stress-driven deformation (as opposed to the strain-driven deformation implemented in this study), lateral extension, uniaxial compression[16] and biaxial deformations.[49] The future directions listed above could provide more insights on the toughening behavior for different chemistries and help to identify viable frameworks for the experimental design of super-tough materials.

The strain-induced recrystallization behavior observed in some of our (experimentally realizable) systems is a potentially beneficial feature that could be exploited in designing shape memory devices and self-healing materials. Indeed, in response to an external force that causes large deformation in the material, the system will not only be able to absorb that energy without generating highly localized bond-breaking stresses that would weaken the material irreversibly, but also be able to recrystallize to maintain the lamella structure and any potential benefits that such morphology may have been intended for. While the material thus deformed will stay deformed for long periods (acting as a shape memory material), the process is reversible and upon heating or compression, the original shape and structure could be partially recovered (as explored in Sec. 3.6). For the purpose of optimizing high-toughness molecular designs, simulations that more directly probe the failure modes and hence the toughness of these materials are also areas of current interest.[22,50]

Supporting Information

Tables for force field parameters, implementation details of guiding field used in section 2.2, summary of force field implementation, plots for time evolution of total bonds and angle energies during crosslinking simulations, reproducibility tests for system 1, stress-strain profile for system 2 and 3, results for six-layer system, additional plots for different strain rates, results for tensile

hysteresis (system 4), NPT equilibration snapshots for all systems, and mean squared displacement (MSD) trends of acrylate sites, RDF and Bond orientation OP implementation and analysis details. Tensile deformation simulation for uncrosslinked (movie S1), system 1 (movie S2), system 4 (movie S3), Evolution of one thiophene layer during deformation for uncrosslinked (movie S4) and system 1 (movie S5)

Author Information

Corresponding Author

Fernando A. Escobedo − Robert Fredrick Smith School of Chemical and Biomolecular Engineering, Cornell University, Ithaca, New York 14853, United States;

Email: fe13@cornell.edu

Acknowledgements

Funding support from NSF DMREF Award No. 1922259 and NSF Award DMR- 2414548 is gratefully acknowledged. This work used the Extreme Science and Engineering Discovery Environment (XSEDE), which is supported by the National Science Foundation Grant No. ACI-1053575. The authors would like to acknowledge Dr. Yangyang Sun for the coarse-grained model and Dr. Vikram Thapar for initial ABA2 configurations and insightful discussions. The authors would also like to thank Dr. Prajwal Bangalore Prakash for Bond orientation order parameter codes and useful discussions regarding crystallization analysis.

REFERENCES

(1) Herbert, K. M.; Fowler, H. E.; McCracken, J. M.; Schlafmann, K. R.; Koch, J. A.; White, T. J. Synthesis and Alignment of Liquid Crystalline Elastomers. *Nat Rev Mater* **2021**, *7* (1), 23–38. https://doi.org/10.1038/s41578-021-00359-z.

(2) Dijkstra, M.; Frenkel, D. Simulation Study of the Isotropic-to-Nematic Transitions of Semiflexible Polymers. *Phys Rev E* **1995**, *51* (6), 5891–5898. https://doi.org/10.1103/PhysRevE.51.5891.
(3) Küpfer, J.; Finkelmann, H. Nematic Liquid Single Crystal Elastomers. *Die Makromolekulare Chemie, Rapid Communications* **1991**, *12* (12), 717–726. https://doi.org/10.1002/marc.1991.030121211.
(4) Gibbons, W. M.; Shannon, P. J.; Sun, S.-T.; Swetlin, B. J. Surface-Mediated Alignment of Nematic Liquid Crystals with Polarized Laser Light. *Nature* **1991**, *351* (6321), 49–50. https://doi.org/10.1038/351049a0.
(5) Brannum, M. T.; Steele, A. M.; Venetos, M. C.; Korley, L. T. J.; Wnek, G. E.; White, T. J. Light Control with Liquid Crystalline Elastomers. *Adv Opt Mater* **2019**, *7* (6). https://doi.org/10.1002/adom.201801683.
(6) Li, M. H.; Keller, P.; Yang, J.; Albouy, P. A. An Artificial Muscle with Lamellar Structure Based on a Nematic Triblock Copolymer. *Advanced Materials* **2004**, *16* (21), 1922–1925. https://doi.org/10.1002/adma.200400658.
(7) Yao, Y.; Waters, J. T.; Shneidman, A. V.; Cui, J.; Wang, X.; Mandsberg, N. K.; Li, S.; Balazs, A. C.; Aizenberg, J. Multiresponsive Polymeric Microstructures with Encoded Predetermined and Self-Regulated Deformability. *Proceedings of the National Academy of Sciences* **2018**, *115* (51), 12950–12955. https://doi.org/10.1073/pnas.1811823115.
(8) Gabert, A. J.; Verploegen, E.; Hammond, P. T.; Schrock, R. R. Synthesis and Characterization of ABA Triblock Copolymers Containing Smectic C* Liquid Crystal Side Chains via Ring-Opening Metathesis Polymerization Using a Bimetallic Molybdenum Initiator. *Macromolecules* **2006**, *39* (12), 3993–4000. https://doi.org/10.1021/ma060243x.
(9) Bu, L.; Qu, Y.; Yan, D.; Geng, Y.; Wang, F. Synthesis and Characterization of Coil−Rod−Coil Triblock Copolymers Comprising Fluorene-Based Mesogenic Monodisperse Conjugated Rod and Poly(Ethylene Oxide) Coil. *Macromolecules* **2009**, *42* (5), 1580–1588. https://doi.org/10.1021/ma802601c.
(10) Terentjev, E. M. Liquid-Crystalline Elastomers. *Journal of Physics: Condensed Matter* **1999**, *11* (24), R239–R257. https://doi.org/10.1088/0953-8984/11/24/201.
(11) Ahir, S. V.; Tajbakhsh, A. R.; Terentjev, E. M. Self-Assembled Shape-Memory Fibers of Triblock Liquid-Crystal Polymers. *Adv Funct Mater* **2006**, *16* (4), 556–560. https://doi.org/10.1002/adfm.200500692.
(12) Rousseau, I. A.; Mather, P. T. Shape Memory Effect Exhibited by Smectic-C Liquid Crystalline Elastomers. *J Am Chem Soc* **2003**, *125* (50), 15300–15301. https://doi.org/10.1021/ja039001s.
(13) Burke, K. A.; Mather, P. T. Soft Shape Memory in Main-Chain Liquid Crystalline Elastomers. *J Mater Chem* **2010**, *20* (17), 3449. https://doi.org/10.1039/b924050k.
(14) Guin, T.; Settle, M. J.; Kowalski, B. A.; Auguste, A. D.; Beblo, R. V.; Reich, G. W.; White, T. J. Layered Liquid Crystal Elastomer Actuators. *Nat Commun* **2018**, *9* (1), 2531. https://doi.org/10.1038/s41467-018-04911-4.
(15) Lee, S.; Rutledge, G. C. Plastic Deformation of Semicrystalline Polyethylene by Molecular Simulation. *Macromolecules* **2011**, *44* (8), 3096–3108. https://doi.org/10.1021/ma1026115.

(16) Kim, J. M.; Locker, R.; Rutledge, G. C. Plastic Deformation of Semicrystalline Polyethylene under Extension, Compression, and Shear Using Molecular Dynamics Simulation. *Macromolecules* **2014**, *47* (7), 2515–2528. https://doi.org/10.1021/ma402297a.
(17) Yeh, I.-C.; Andzelm, J. W.; Rutledge, G. C. Mechanical and Structural Characterization of Semicrystalline Polyethylene under Tensile Deformation by Molecular Dynamics Simulations. *Macromolecules* **2015**, *48* (12), 4228–4239. https://doi.org/10.1021/acs.macromol.5b00697.
(18) Yeh, I.-C.; Lenhart, J. L.; Rutledge, G. C.; Andzelm, J. W. Molecular Dynamics Simulation of the Effects of Layer Thickness and Chain Tilt on Tensile Deformation Mechanisms of Semicrystalline Polyethylene. *Macromolecules* **2017**, *50* (4), 1700–1712. https://doi.org/10.1021/acs.macromol.6b01748.
(19) Ranganathan, R.; Kumar, V.; Brayton, A. L.; Kröger, M.; Rutledge, G. C. Atomistic Modeling of Plastic Deformation in Semicrystalline Polyethylene: Role of Interphase Topology, Entanglements, and Chain Dynamics. *Macromolecules* **2020**, *53* (12), 4605–4617. https://doi.org/10.1021/acs.macromol.9b02308.
(20) Aguilera-Mercado, B. M.; Cohen, C.; Escobedo, F. A. Sawtooth Tensile Response of Model Semiflexible and Block Copolymer Elastomers. *Macromolecules* **2014**, *47* (2), 840–850. https://doi.org/10.1021/ma4020998.
(21) Nowak, C.; Escobedo, F. A. Tuning the Sawtooth Tensile Response and Toughness of Multiblock Copolymer Diamond Networks. *Macromolecules* **2016**, *49* (17), 6711–6721. https://doi.org/10.1021/acs.macromol.6b00733.
(22) Nowak, C.; Escobedo, F. A. Optimizing the Network Topology of Block Copolymer Liquid Crystal Elastomers for Enhanced Extensibility and Toughness. *Phys Rev Mater* **2017**, *1* (3), 035601. https://doi.org/10.1103/PhysRevMaterials.1.035601.
(23) Nowak, C.; Escobedo, F. A. Effect of Block Immiscibility on Strain-Induced Microphase Segregation and Crystallization of Model Block Copolymer Elastomers. *Macromolecules* **2018**, *51* (15), 5685–5693. https://doi.org/10.1021/acs.macromol.8b00965.
(24) Song, Y.; Liu, Y.; Qi, T.; Li, G. L. Towards Dynamic but Supertough Healable Polymers through Biomimetic Hierarchical Hydrogen-Bonding Interactions. *Angewandte Chemie* **2018**, *130* (42), 14034–14038. https://doi.org/10.1002/ange.201807622.
(25) Smith, B. L.; Schäffer, T. E.; Viani, M.; Thompson, J. B.; Frederick, N. A.; Kindt, J.; Belcher, A.; Stucky, G. D.; Morse, D. E.; Hansma, P. K. Molecular Mechanistic Origin of the Toughness of Natural Adhesives, Fibres and Composites. *Nature* **1999**, *399* (6738), 761–763. https://doi.org/10.1038/21607.
(26) King, D. R.; Okumura, T.; Takahashi, R.; Kurokawa, T.; Gong, J. P. Macroscale Double Networks: Design Criteria for Optimizing Strength and Toughness. *ACS Appl Mater Interfaces* **2019**, *11* (38), 35343–35353. https://doi.org/10.1021/acsami.9b12935.
(27) Ruiz, C.; García-Frutos, E. M.; Hennrich, G.; Gómez-Lor, B. Organic Semiconductors toward Electronic Devices: High Mobility and Easy Processability. *J Phys Chem Lett* **2012**, *3* (11), 1428–1436. https://doi.org/10.1021/jz300251u.
(28) Liu, Z.; Dong, B. X.; Misra, M.; Sun, Y.; Strzalka, J.; Patel, S. N.; Escobedo, F. A.; Nealey, P. F.; Ober, C. K. Self-Assembly Behavior of an Oligothiophene-Based Conjugated Liquid Crystal and Its Implication for Ionic Conductivity Characteristics. *Adv Funct Mater* **2019**, *29* (2), 1805220. https://doi.org/10.1002/adfm.201805220.

(29) Dong, B. X.; Liu, Z.; Misra, M.; Strzalka, J.; Niklas, J.; Poluektov, O. G.; Escobedo, F. A.; Ober, C. K.; Nealey, P. F.; Patel, S. N. Structure Control of a π-Conjugated Oligothiophene-Based Liquid Crystal for Enhanced Mixed Ion/Electron Transport Characteristics. *ACS Nano* **2019**, *13* (7), 7665–7675. https://doi.org/10.1021/acsnano.9b01055.

(30) Wang, Z.; Wang, C.; Sun, Y.; Wang, K.; Strzalka, J. W.; Patel, S. N.; Nealey, P. F.; Ober, C. K.; Escobedo, F. A. Ion Transport in 2D Nanostructured π-Conjugated Thieno[3,2- *b*]Thiophene-Based Liquid Crystal. *ACS Nano* **2022**, *16* (12), 20714–20729. https://doi.org/10.1021/acsnano.2c07789.

(31) Misra, M.; Liu, Z.; Dong, B. X.; Patel, S. N.; Nealey, P. F.; Ober, C. K.; Escobedo, F. A. Thermal Stability of π-Conjugated *n* -Ethylene-Glycol-Terminated Quaterthiophene Oligomers: A Computational and Experimental Study. *ACS Macro Lett* **2020**, *9* (3), 295–300. https://doi.org/10.1021/acsmacrolett.9b00935.

(32) Sun, Y. Computational Study of Self-Assembly of Amphiphilic and Polyphilic Molecules and Application in Li-Ion Transport, Ph.D. Dissertation, Cornell University, Ithaca, NY , 2023. https://doi.org/10.7298/1jt5-c871.

(33) Thompson, A. P.; Aktulga, H. M.; Berger, R.; Bolintineanu, D. S.; Brown, W. M.; Crozier, P. S.; in 't Veld, P. J.; Kohlmeyer, A.; Moore, S. G.; Nguyen, T. D.; Shan, R.; Stevens, M. J.; Tranchida, J.; Trott, C.; Plimpton, S. J. LAMMPS - a Flexible Simulation Tool for Particle-Based Materials Modeling at the Atomic, Meso, and Continuum Scales. *Comput Phys Commun* **2022**, *271*, 108171. https://doi.org/10.1016/j.cpc.2021.108171.

(34) Plimpton, S. Fast Parallel Algorithms for Short-Range Molecular Dynamics. *J Comput Phys* **1995**, *117* (1), 1–19. https://doi.org/10.1006/jcph.1995.1039.

(35) Gissinger, J. R.; Jensen, B. D.; Wise, K. E. Modeling Chemical Reactions in Classical Molecular Dynamics Simulations. *Polymer* **2017**, *128*, 211–217. https://doi.org/10.1016/j.polymer.2017.09.038.

(36) Torres-Knoop, A.; Kryven, I.; Schamboeck, V.; Iedema, P. D. Modeling the Free-Radical Polymerization of Hexanediol Diacrylate (HDDA): A Molecular Dynamics and Graph Theory Approach. *Soft Matter* **2018**, *14* (17), 3404–3414. https://doi.org/10.1039/C8SM00451J.

(37) Karnes, J. J.; Weisgraber, T. H.; Oakdale, J. S.; Mettry, M.; Shusteff, M.; Biener, J. On the Network Topology of Cross-Linked Acrylate Photopolymers: A Molecular Dynamics Case Study. *J Phys Chem B* **2020**, *124* (41), 9204–9215. https://doi.org/10.1021/acs.jpcb.0c05319.

(38) Moon, J.; Kim, B.; Choi, J.; Cho, M. Multiscale Study of the Relationship between Photoisomerization and Mechanical Behavior of Azo-Polymer Based on the Coarse-Grained Molecular Dynamics Simulation. *Macromolecules* **2019**, *52* (5), 2033–2049. https://doi.org/10.1021/acs.macromol.8b02535.

(39) Xie, H.; Basu, S.; DeMeter, E. C. Molecular Dynamics Simulations of Photo-Induced Free Radical Polymerization. *J Chem Inf Model* **2020**, *60* (12), 6314–6327. https://doi.org/10.1021/acs.jcim.0c01156.

(40) Moad, G.; Solomon, D. H. *The Chemistry of Radical Polymerization*, 2nd ed.; Elsevier, 2005. https://doi.org/10.1016/B978-0-08-044288-4.X5015-8.

(41) Odian, G. *Principles of Polymerization*, 4th ed.; John Wiley And Sons, 2004. https://doi.org/10.1002/047147875X.

(42) Makke, A.; Lame, O.; Perez, M.; Barrat, J.-L. Nanoscale Buckling in Lamellar Block Copolymers: A Molecular Dynamics Simulation Approach. *Macromolecules* **2013**, *46* (19), 7853–7864. https://doi.org/10.1021/ma400514h.
(43) Sami, S.; Marrink, S. J. Reactive Martini: Chemical Reactions in Coarse-Grained Molecular Dynamics Simulations. *J Chem Theory Comput* **2023**, *19* (13), 4040–4046. https://doi.org/10.1021/acs.jctc.2c01186.
(44) Park, S.; Moon, J.; Kim, B.; Cho, M. Multi-Scale Coarse-Grained Molecular Dynamics Simulation to Investigate the Thermo-Mechanical Behavior of Shape-Memory Polyurethane Copolymers. *Polymer* **2021**, *213*, 123228. https://doi.org/10.1016/j.polymer.2020.123228.
(45) Steinhardt, P. J.; Nelson, D. R.; Ronchetti, M. Bond-Orientational Order in Liquids and Glasses. *Phys Rev B* **1983**, *28* (2), 784–805. https://doi.org/10.1103/PhysRevB.28.784.
(46) De Gennes, P.-G.; Prost, J. *The Physics of Liquid Crystals*; Oxford university press, 1993.
(47) Adhikari, R.; Michler, G. H. Influence of Molecular Architecture on Morphology and Micromechanical Behavior of Styrene/Butadiene Block Copolymer Systems. *Prog Polym Sci* **2004**, *29* (9), 949–986. https://doi.org/10.1016/j.progpolymsci.2004.06.002.
(48) Makke, A.; Perez, M.; Lame, O.; Barrat, J.-L. Nanoscale Buckling Deformation in Layered Copolymer Materials. *Proceedings of the National Academy of Sciences* **2012**, *109* (3), 680–685. https://doi.org/10.1073/pnas.1111367109.
(49) Tu, Y.; Shi, P.; Liu, D.; Wen, R.; Yu, Q.; Sas, G.; Elfgren, L. Mechanical Properties of Calcium Silicate Hydrate under Uniaxial and Biaxial Strain Conditions: A Molecular Dynamics Study. *Physical Chemistry Chemical Physics* **2022**, *24* (2), 1156–1166. https://doi.org/10.1039/D1CP04474E.
(50) Zhao, R.; Wang, Y.; Gong, X. Fracture Behaviors of Double Network Elastomers with Dynamic Non-Covalent Linkages: A Molecular Dynamics Study. *Polymer* **2022**, *244*, 124670. https://doi.org/10.1016/j.polymer.2022.124670.

FOR TABLE OF CONTENTS ONLY: